Time resolution in cryo-EM using a novel PDMS-based microfluidic chip assembly and its application to the study of HflX-mediated ribosome recycling

Sayan Bhattacharjee[1,#], Xiangsong Feng[1,#*], Suvrajit Maji[1], Prikshat Dadhwal[2], Zhening Zhang[1], Zuben P. Brown[1,3], Joachim Frank[1,2*†].

[1]Department of Biochemistry and Molecular Biophysics, Columbia University, New York, NY 10027, USA

[2]Department of Biological Sciences, Columbia University, New York, NY 10027, USA

[3]Current address: Thermo Fisher Scientific, Oregon, USA

[#]These authors contributed equally

[*] Corresponding Authors

[†]Lead Contact

The rapid kinetics of biological processes and associated short-lived conformational changes pose a significant challenge in attempts to structurally visualize biomolecules during a reaction in real time. Conventionally, on-pathway intermediates have been trapped using chemical modifications or reduced temperature, giving limited insights. Here we introduce a novel time-resolved cryo-EM method using a reusable PDMS-based microfluidic chip assembly with high reactant mixing efficiency. Coating of PDMS walls with SiO_2 virtually eliminates non-specific sample adsorption and ensures maintenance of the stoichiometry of the reaction, rendering it highly reproducible. In an operating range from 10 to 1000 ms, the device allows us

to follow in vitro reactions of biological molecules at resolution levels in the range of 3 Å. By employing this method, we show for the first time the mechanism of progressive HlfX-mediated splitting of the 70S *E. coli* ribosome in the presence of the GTP, via capture of three high-resolution reaction intermediates within 140 ms.

Introduction

To comprehend the fundamentals of any biological process, one requires insights into the underlying molecular mechanisms. It is often possible to study a reaction in vitro, outside the context of the cell. However, interactions among reactants and concurrent conformational changes of the molecules are too fast to be captured structurally using standard methods of biophysical imaging. In single-particle cryo-EM, the conventional pipetting-blotting method of sample deposition on the grid requires several seconds at least -- too long to capture reaction intermediates of molecular machines, which are in the range of tens or hundreds of milliseconds. In the past, some of such intermediates have been trapped by the use of non-hydrolysable analogs (such as GMP-PNP[1,2], antibiotics[3], or cross-linking[4]), but the insights gained in this way are limited and often burdened with presumptions.

Time-resolved cryo-EM (TRCEM) opens a way for obtaining structural and kinetic information on reaction systems that are not in equilibrium but change over time until equilibrium is reached[5]. In TRCEM studies, the biological reaction is started by mixing reactants, then stopped at a selected time point by fast-freezing, and the so trapped reaction intermediates are

visualized by single-particle cryo-EM. By means of multiple experiments with different time points, TRCEM is able to capture the time course of a reaction, leading to a 'movie' of intermediates on the path to the state in equilibrium[6].

Over the years, a variety of TRCEM methods have been developed[7-19] showing the potential for obtaining key insights into the mechanism of action of molecules and molecular machines on the time scale of tens to hundreds of milliseconds. These methods can be divided into two categories: spraying/mixing[15] and mixing/spraying[10]. In the first category, a specialized sprayer[15] or dispenser system[7] is employed to deposit one reactant onto a grid already covered with another reactant. Both mixing and reacting occur on the grid immediately prior to vitrification. Questions have been raised over the uniformity of a diffusion-dependent reaction on the grid[6]. In addition, electron tomography has shown that molecules are frequently observed to congregate at the top and bottom of the ice layer[20], raising concerns about artifacts stemming from their extended exposure to the air-water interface in spraying/mixing or dispensing/mixing methods. In the second category, a microfluidic chip is used for mixing and reacting two reactants and for subsequent rapid spraying to deposit the reaction product onto the grid, followed immediately by plunging of the grid into the cryogen[8-10,12-14,16]. In that case, mixing and reacting can be efficiently controlled, and the time during which the reaction product is exposed to the air-water interface is kept minimal.

There are still some key issues among the existing methods which need to be resolved. One problem is sample adsorption on the walls of the chip. Polymers such as PDMS, IP-S, IP-Q are now commonly used as a cost-

77 effective material to fabricate microfluidic chips[12,13,18,19], but as a rule, the
78 surfaces of these materials are intrinsically hydrophobic and adsorb a
79 substantial amount of protein. In this case, the contact between the sample and
80 the polymer microchannel can degrade the quality of the reaction, casting
81 doubt over the accuracy of the kinetic information. This problem is avoided
82 with silicon-based microfluidic chips[16,17] which are by nature hydrophilic, but
83 they are quite impractical as it takes several weeks and on average hundreds of
84 dollars to manufacture a chip of a specific design (i.e., in multiple copies; with
85 production steps including the etching and dicing of a silicon wafer and
86 bonding it with glass). Another problem is insufficient initiation of a reaction,
87 which may result from ineffective mixing of fluids due to limited micromixer
88 performance[12,14] in the laminar flow regime.

89 In the following we describe our TRCEM setup utilizing a PDMS-based
90 microfluidics chip assembly of new design that overcomes these problems, as
91 it efficiently mixes the reactants for uniform initiation of a reaction, conducts
92 a controlled reaction virtually unimpeded by protein adsorption, and sprays the
93 reaction product in a uniform three-dimensional cone onto the EM grid. We
94 have used this novel device successfully in several studies on translation. Here
95 we present the study of HflX-mediated recycling in detail to demonstrate the
96 efficacy of the novel TR device, and its capability to yield biologically
97 significant information.

98 **H**igh **f**requency of **l**ysogenization **X** (HflX) is a universally conserved
99 protein for prokaryotes, a GTPase which acts as a ribosome-splitting factor in
100 response to heat shock or antibiotics[2,21-23]. *E. coli* HflX consists of four
101 domains: N-terminal domain (NTD), GTP binding domain (GBD), C-terminal

102 domain (CTD), and helical linker domain (HLD)[2,24]. The cryo-EM structure of
103 the HflX-50S complex stalled in the presence of GMP-PNP, a non-
104 hydrolysable GTP analog, revealed that the HLD and NTD of HflX bind to the
105 peptidyl-transferase center, presumably causing rupture of the intersubunit
106 bridge B2a (h44:H69), thereby promoting the dissociation of the 70S
107 ribosome[2]. However, the molecular mechanism of these events and particularly
108 the interaction between HflX and 70S have remained elusive. Using TRCEM,
109 we were able to capture three short-lived intermediate states, at resolutions in
110 the 3-Å range, by starting the reaction between HflX and the *E. coli* 70S
111 ribosome in the presence of GTP and stopping it at 10, 25 and 140 ms. Atomic
112 models of these states allowed us to elucidate the mechanism of this process in
113 great detail.
114

115 **Results**

116 **A novel microfluidic chip assembly for TRCEM**

117 The complete setup for TRCEM grid preparation, originally based on an
118 apparatus built by Howard White[25], is depicted in Figure S2. The heart of the
119 TR apparatus is the microfluidic chip assembly mounted next to the plunger
120 (Figure 1A), which are both accommodated in an environmental chamber that
121 maintains the temperature and humidity at controllable levels. The plunger,
122 which is pneumatically operated, holds the tweezers on which the EM grid is
123 mounted for fast plunging into liquid ethane after passing the spray cone. In
124 addition, the apparatus contains the pumping system for introducing the
125 solutions into the micro-mixer and the nitrogen gas into the gas inlets of the

126 micro-sprayer. Finally it also houses the computer for controlling both the
127 pumping system and the plunger.

128 We designed and successfully tested the modular TR chip assembly
129 shown in Figure 1B, which is composed of three elements/modules: 1) a SiO_2-
130 coated, PDMS-based splitting-and-recombination (SAR) micro-mixer with 3D
131 self-crossing channels (Figure 1C), which is able to mix the solutions with the
132 effectiveness of > 90% at working flowrate of 6 μL/s (Figures 1E and S3, and
133 Methods section in Supplemental Information(SI)); 2) a micro-capillary glass
134 tubing serving as the micro-reactor for stable (i.e., unchanged under conditions
135 of high pressure drop) reaction time control (Figure S4, and Methods section
136 in SI); 3) a PDMS-based micro-sprayer with inner capillary tubing for spraying
137 out the reaction product under the action of pressurized nitrogen gas (Figure
138 1F, Methods section in SI, and supplemental video 1).

139 To prevent adsorption of molecules, plasma-enhanced chemical vapor
140 deposition (PECVD) is used to coat the inside walls of the PDMS micro-mixer
141 channels with a thin SiO_2 layer. We tested the sample adsorption with the *E.*
142 *coli* 70S ribosome to compare the chips without coating to those with DDM or
143 SiO_2 coating. The sample concentration in buffer is measured before and after
144 passing the devices with different types of coatings by our Nanodrop UV-Vis
145 Spectrophotometer (see Methods section in SI). In this experiment, 94% of the
146 initial concentration was retained using the SiO_2-coated chip (Figure 1H and
147 Table S2), while only 54% and 60% were retained after the sample was passed
148 through the chip assembly without coating or with DDM coating, respectively.
149 These findings demonstrate that the SiO_2 coating can effectively mitigate the
150 sample adsorption for ribosomes. After one month, the SiO_2-coated chip

151 assembly was tested again with 70S ribosome and HflX protein, and 92% of
152 the 70S and 93% of HflX were shown to be still retained, respectively (Figure
153 1I). These results demonstrate that the hydrophilicity of the internal surface is
154 virtually undiminished after a substantial period of time.

155 Thus it is apparent that the solutions introduced from the glass-capillary
156 liquid inlets will pass through the entire microfluidic device (SiO_2-coated
157 micromixer, glass-capillary micro-reactor and glass-capillary inner tubing of
158 the micro-sprayer) without contact with any hydrophobic surface, a fact of high
159 importance for preserving the stoichiometry of a reaction and guaranteeing its
160 reproducibility.

161 Based on these initial test results, we fabricated a set of microfluidic
162 chips (Figure 1G) to conduct a set of biological experiments. The relevant
163 materials and parameters for the fabrication of the chip assemblies are listed in
164 Table S1. An estimation of reaction times achieved using this TRCEM method
165 in the application to HflX-mediated ribosome recycling is given in the Methods
166 section in SI. Four microfluidic chip assemblies were used, with reaction times
167 estimated to be 10, 25, 140, and 900 ms, respectively.

168

169 **Exposure-targeting strategy in data collection for droplets-based cryo-**
170 **grids**

171 For grids obtained by the conventional blotting method, data collection is
172 usually done automatically after the template is set up for targeting both the
173 holes and exposures. But for grids prepared by the mixing-spraying method, it
174 is not easy to use automation, since every collectible square possesses droplets

of different sizes and thicknesses[25]. Hence time-consuming manual exposure targeting is required.

Some observations on typical particle distributions in the HflX experiment, to be detailed below, and other experiments led us to develop an effective strategy for exposure targeting in data collection on droplet-based grids.

There are two types of situations: one is where the droplet has no contact with the grid bar (marked red in Figure S8); and the other where it does have contact with the grid bar (marked green in Figure S8). In the former, the ice is observed to be thick and unsuitable for data collection, while in the latter, there is always some part of the region near the grid bar with an ice thickness suitable for data collection. All our exposure targets are therefore focused on the second type of droplets, as detailed below.

In the beginning, as shown in Figure 2A, we tried to collect data on as many holes as possible for droplets of the second category, i.e., touching or partially covering the grid bar, and found that typically there are four regions with different behaviors, following a trend: (i) very close to the grid bar, as in the area marked blue, the ice is not vitrified very well but particles are still visible; (ii) in the area marked cyan, particles are clearly visible; (iii) further on, in the area marked yellow, the number of the particles has significantly decreased; until, (iv) in the area marked red, there are almost no particles left (Figure 2A). In the present instance of data collection, only 170 out of 580 micrographs, or 29%, were left for data processing.

In line with these observations, we developed the exposure-targeting strategy shown in Figure 2B: we collect only along two or three lines of holes

200 which are near and parallel to the grid bar, in the areas of type (i), (ii) and (iii).
201 As a result, in our example, we obtained 3433 good micrographs out of a 4458
202 total, which means about 77% could be used in this case for data processing.
203 We therefore adopted this strategy for all our data collection on grids prepared
204 by TR cryo-EM.
205

206 **Time-resolved experiments on HflX-mediated ribosome recycling from 10**
207 **to 900 ms**

208 HflX acts on the 70S ribosome in a nucleotide-dependent way, and light
209 scattering analysis revealed that the rate of ribosome splitting by HflX-GTP
210 (0.002 s^{-1}) is very similar to the rate of ribosome dissociation by the combined
211 action of RRF and EF-G-GTP (0.005 s^{-1})[22,26]. The fraction of ribosomes split
212 into subunits at room temperature within a reaction time of 140 ms is close to
213 50%, according to our earlier TR cryo-EM experiment on *E. coli* ribosome
214 recycling in the presence of RRF, EF-G, and GTP[9]. In view of these findings,
215 we anchored our TR cryo-EM study at a 140 ms reaction time point and added
216 two shorter time points (10 ms and 25 ms) and one longer one (900 ms) toward
217 the reaction's completion. We mixed 70S ribosomes with the HflX-GTP
218 complex in our mixing-spraying TRCEM apparatus (Figure S2) using different
219 microfluidic chips of the PDMS-based design (Figure 1G and Methods section
220 in SI). As in our previous TRCEM studies[9,10], 3D classification was performed
221 on the entire, pooled dataset across all four time points. The 3D classification
222 produced seven distinct classes, which we characterized by examining the
223 corresponding reconstructed density maps (note: "rotated" and "nonrotated"
224 refers in the following to the presence or absence of intersubunit rotation[27]):

225 (1) rotated 70S without HflX ($r70S_{noHflX}$); (2) non-rotated 70S without HflX
226 ($nr70S_{noHflX}$); (3) 70S-like intermediate-I with HflX ($i70S_{HflX}$-I); (4) 70S like-
227 intermediate-II with HflX ($i70S_{HflX}$-II); (5) 70S-like intermediate-III with HflX
228 ($i70S_{HflX}$-III); (6) 50S with HflX ($50S_{HflX}$); and (7) 30S (Methods section in SI
229 and Figures S10, and S11).

230 The splitting reaction kinetics of the 70S ribosome, as evaluated by
231 counting the numbers of particles obtained upon 3D classifications from 10 ms
232 to 900 ms, is found to follow a similar, roughly exponential behavior as
233 reported from dissociation kinetics measured by light scattering[2] (Figure 3M).
234 Furthermore, we noticed a rapid increase in the number of free 30S subunit
235 particles from 140 ms to 900 ms, which leads us to conclude that the final
236 separation of the subunits commences not earlier than with state $i70S_{HflX}$-III
237 (Figure 3M).

238

239 **Intermediate states of HflX-mediated recycling and their interpretation**

240 The three classes of HflX-containing intermediates and class $50S_{HflX}$ -- four of
241 the seven 3D classes we found -- were selected for additional structural
242 analysis (Methods section in SI and Figures S10, and S11A-E). Furthermore,
243 focused 3D classification and subsequent reconstruction of HflX-binding
244 regions from each of the resulting class reconstructions yielded high-resolution
245 density maps for four states of HflX: (1) HflX-I, (2) HflX-II, (3) HflX-III, and
246 (4) HflX-IV (Figure S10). Refinement on the three $i70S_{HflX}$ class
247 reconstructions yielded high-resolution on-pathway intermediates $i70S_{HflX}$-I,
248 $i70S_{HflX}$-II, and $i70S_{HflX}$-III (Figures 3A-H), and their resolutions are indicated
249 in Figure S12 and Table S3. The kinetics of the reaction can be followed from

250 the histogram of particle counts in the respective classes (Figure 3M). The
251 intermediates i70S$_{HflX}$-I, i70S$_{HflX}$-II, and i70S$_{HflX}$-III are each dominant in the
252 10 ms, 25 ms, and 140 ms time points, respectively, but are always intermixed
253 with the other intermediates, as well as with apo-70S, and the 50S-HflX end
254 product.

255 In all three intermediates, the CTD of HflX is found anchored to uL11
256 of the 50S subunit at the bL12 stalk base. Overall the comparison of the
257 intermediates shows a gradual clamshell-like opening of the 70S ribosome (see
258 supplemental video 2).

259 Structurally, the intermediates are distinguished by (i) the degree of the
260 clamshell-like opening, (ii) the position of helix H69 (in two steps, from
261 i70S$_{HflX}$-I to -III), (iii) the position of helix H71 (from i70S$_{HflX}$-I to -II), and
262 (iv) the position of HflX with respect to the 50S subunit (from i70S$_{HflX}$-I to -II,
263 and reversed from -II to -III). In the final state observed, after the departure of
264 the 30S subunit, HflX remains bound to the 50S subunit.

265 Comparison of the atomic models obtained for these intermediates with
266 one another and with the apo-70S revealed that the opening and splitting of the
267 70S ribosome occurs in the following steps:

268 First, the ribosome opens slightly to accommodate the initial binding of
269 HflX in i70S$_{HflX}$-I (Figures 3A, 3E-F). Using the tool previously developed[28]
270 we find that in this first intermediate, the 30S subunit has rotated by 5.9°
271 around an axis (Axis I) that passes through the intersubunit bridges B1b, B2a,
272 B3, and B4 (Figures 6A, D, G, and 6J-K), and this rotation has moved protein
273 bS6 of 30S into close vicinity to protein uL2 of the 50S subunit (Figures 3I-J).
274 Apparently, the insertion of HflX along with the prying apart of the 70S

275 ribosome and the rotation of the 30S subunit is driven by the increase in
276 backbone entropy of uL2 in i70S$_{HflX}$-I compared to apo-70S since we find
277 indications of disorder: the density of uL2 is not resolved well in i70S$_{HflX}$-I
278 (Figure 3J) compared to all its other manifestations in apo-70S, i70S$_{HflX}$-II and
279 i70S$_{HflX}$-III (Figures 3I-J, and S13). Comparison of the 50S subunit in i70S$_{HflX}$-
280 I and apo-70S shows that H69 has moved by 6.7 Å, apparently through a push
281 by HflX since fitting the model of HflX to apo-70S reveals a steric clash with
282 H69 (Figure 3K-L). In i70S$_{HflX}$-I HflX is blurred, indicating motion-induced
283 heterogeneity of the population in that class (Figure S10).

284 Going from this first intermediate to i70S$_{HflX}$-II and i70S$_{HflX}$-III we
285 observe stepwise rotations, by 7.9° and 8.2°, respectively, of the 30S subunit
286 around a new axis (Axis II) passing through intersubunit bridges B3 and B7a,
287 which are both located along helix h44 (Figures 3B-C, 3F-H, and 6B-C, 6E-F,
288 6H-I, and 6J-K). In the first step of rotation around this new axis, protein bS6
289 moves away from protein uL2 (Figures 3B, 3F-G, and 6B, 6E, 6H, and 6J-K).
290 This movement is made possible by a 6.5-Å pull of C1965 of H71 as a result
291 of HflX moving from its previous position on i70S$_{HflX}$-I to a new position on
292 i70S$_{HflX}$-II and a subsequent shift of the loop-helix motif (G74-V100)
293 associated with the NTD of HflX (Figures 4D-G). As a consequence, bridge
294 B3 (h44:H71), as well as bridges B7b and B7bR, have become destabilized.
295 While the conformation of the 30S subunit remains virtually the same from
296 apo-70S to the first intermediate, the change from the first to second
297 intermediate is accompanied by a rotation of the 30S subunit head by 2.1°
298 around another axis, Axis III (Figure S14).

299 In the second step of the 30S subunit rotation around Axis II, from
300 i70S$_{HflX}$-II to i70S$_{HflX}$-III, protein bS6 has continued to move away from
301 protein uL2 (Figure 3C, 3F-H, and 6C, 6F, 6I, and 6J-K), and HflX has shifted
302 back to its original position on the 70S ribosome in i70S$_{HflX}$-I. Bridges B7b and
303 B7bR are now entirely disrupted, allowing the flexible loop (E323-G349) of
304 HflX's GTD to readily access the 30S subunit protein uS12, thus positioned to
305 jettison the 30S subunit from the 70S ribosome (Figure 4A-C).

306 Finally, the reconstruction of the stable 50S-HflX complex, at 3.6-Å
307 resolution (Figures 3D, and S15A), no longer shows any trace of density from
308 the 30S subunit (Figures S15A, and D). This class mainly contains particles
309 from 900 ms (Figure 3M). The map agrees quite well with the map of HflX-
310 50S-GNP-PNP[2] (Figures S15A-C).

311 A comparison of the atomic models built for the three intermediate states
312 reveals that HflX changes its position on the ribosome and undergoes major
313 conformational changes, specifically in its CTD, HLD, and NTD. The domain
314 movements of CTD and HLD match quite well with the dynamics of apo-HflX
315 predicted from 1000 ns of molecular dynamics simulations (Methods section
316 in SI and Figure S16). Interestingly, the loop-helix motif (G74-V100) of NTD
317 makes stable contact with H71 of the 50S subunit in i70S$_{HflX}$-II (Figures 4D-
318 F).

319

320 **Dynamics of HflX and possible GTP-bound state**

321 In trying to understand the actions of HflX, we examined the hydrolyzation
322 state of GTP in the different states of HflX. At 25 ms, with the exception of
323 their NTDs, the densities of HflX and associated nucleotides in states HflX-I

324 and HflX-II are not resolved as well as they are for the other two states,
325 indicating mobility and preventing determination of the hydrolyzation state
326 (Figure S10). In an attempt to fit the atomic model of GTP to the corresponding
327 densities in HflX-III and HflX-IV, we observed that the density in the region
328 of the nucleotide site on HflX-III is a better fit for GDP·Pi than for either GTP
329 or GDP (Figure 5A). A similar matching effort resulted in a decent match of
330 GTP to the density of HflX bound to the 50S subunit, even though the GDP
331 state is expected to be found at this stage (Figure 5B).

332 Since at the 140 ms time point the inorganic phosphate (Pi) is still
333 associated with GDP and virtually none of the 30S subunits has been cleaved
334 off, we conclude that the energy for the breaking of bridges B3 and B7a and
335 the final dissociation of the 30S subunit is set free by the release of Pi. It is
336 unclear without further investigation if GTP hydrolysis plays a role in the
337 initial stages of splitting, from intermediate I to II, since it is known that HflX
338 can perform the splitting in the absence of GTP, albeit at a slower rate[2]. The
339 likely explanation for the observation of GTP on the 50S subunit-bound HflX
340 molecule at 900 ms is that by that time both Pi and GDP have left and that a
341 new GTP molecule has taken their place.

342

343 **Time-dependent rupturing of intersubunit bridges**

344 As the direct observation of the state of bridges from the cryo-EM map is not
345 conclusive due to resolution limitations, we proceeded with a geometric
346 calculation to estimate the sequence in which intersubunit bridges are ruptured.
347 With the axes and angles of the 30S subunit rotation known, as well as the
348 locations of all bridges relative to the axes, we were able to determine the

349 distances between constituent residues of all intersubunit bridges. From these
350 distances and known ranges of chemical bond lengths we were able to estimate
351 at which time points the intersubunit bridges are likely disrupted and broken
352 (Figure 5D). According to these calculations, bridges B1a, B1b, B2a, and B2b
353 are already disrupted at 10 ms. Bridges B5, B6, B7b, and B7bR are disrupted
354 between 10 and 25 ms. All these bridges are found to be broken within 140 ms.
355 Finally, the last two bridges, B3 and B7a, which form the hinges of Axis II,
356 give way at some time point between 140 ms and 900 ms. Bridge B4
357 (H34:uS15) presents an interesting case as it behaves like a spring: its 50S
358 subunit constituent H34 is initially compressed in the step from apo-70S to
359 $i70S_{HflX}$-I, as HflX is accommodated within the first 10 ms, but in the next two
360 steps (10 ms to 25 ms to 140 ms) it is extended (Figure 5C). This bridge finally
361 breaks along with B3 and B7a after 140 ms and, in $50S_{HflX}$, helix H34 has
362 returned to its original position as in apo-70S.
363

364 **Discussion**

365 Here, we present a method for preparing time-resolved cryo-EM grids to
366 capture intermediates on the ~10 to 1,000-ms timescale. Different in design
367 from those by Lu et al.[16,17], Mäeotset al.[13], and Kontziampasis et al.[14], the
368 microfluidic chip assembly comprises three replaceable modules: (1) a PDMS-
369 based internally SiO_2-coated micro-mixer of the splitting-and-recombination
370 (SAR) type, for efficiently mixing two samples without significant problems
371 from protein adsorption; (2) a glass capillary micro-reactor for defining the
372 reaction time, and (3) a PDMS-based micro-sprayer for depositing the reaction
373 product onto the EM-grid. The sample is subsequently vitrified by fast

374 plunging of the grid into the cryogen so that the TR cryo-grid can be well
375 prepared.
376
377 In our application to the study of HflX-mediated ribosome recycling, a
378 bacterial defense response to stress, we have demonstrated how our method is
379 able to capture, on-the-fly, high-resolution structures of intermediates that
380 represent snapshots of an unfolding complex molecular mechanism. Based on
381 our cumulative observations from the examination of three short-lived reaction
382 intermediates, we propose that the initial binding of HflX within 10 ms is
383 followed by a stepwise clamshell-like opening of the ribosome around an axis
384 that closely aligns with helix 44 of the 30S subunit, and that rupture of the last
385 two remaining intersubunit bridges, B3 and B7a, occurs after 140 ms and most
386 probably as a result of Pi release.
387
388 **Further applications of time-resolved cryo-EM in the study of functional**
389 **dynamics**
390 Our study will spur interest in the community for extending these studies to
391 recycling in the 80S ribosome by protein factors such as ABCE1 to structurally
392 reveal an evolutionarily conserved mechanism. We believe, moreover, that the
393 quantitative description of our results on a dynamic process – employing tensor
394 analysis to determine the tilt axis and rotation of subunits, and quantifying the
395 timing of intersubunit breakage – as well as the application of this microfluidic
396 device will open a new direction in the characterization of molecular events by
397 cryo-EM and will stimulate interest and draw considerable attention among a
398 wide audience of structural biologists, microbiologists, and pharmacologists.

399 Ultimately, it may help in the design of a new class of broad-spectrum
400 antibiotics that are able to overcome antibiotic resistance.
401
402 **Limitations of the Study**
403
404 **Limitation in time range:** Our method of TRCEM has been proven powerful
405 for capturing structural intermediates for HflX-mediated ribosome recycling
406 and other processes of translation, but there are many other interesting
407 biochemical processes awaiting visualization by this method. Those involving
408 motions of large domains of macromolecules are excellent candidates.
409 Signaling, activation and gating mechanisms of receptors and transporters[29-31]
410 come to mind, as well, but in many cases the characteristic times of motions
411 are much shorter than 10 ms, the minimum reached by our method of mixing-
412 spraying-plunging. In this time domain, entirely different technologies have to
413 be considered[15,19,32,33]
414
415 **Limitation in the accuracy of kinetic information.** As we pointed out
416 before[10], TRCEM, in addition to furnishing the high-resolution structures of
417 reaction intermediates, has at least in principle the capacity to give kinetic
418 information, as well, since the numbers of particles in each structural class are
419 known. However, this information is currently not very accurate since it
420 depends on the vagaries of particle picking and classification strategies.
421 Investment in a search for quantitative, reproducible strategies would therefore
422 be of enormous value.
423

424 **Inefficiency of data collection.** Data collection on droplet-covered TRCEM
425 grids remains quite time-consuming even with the proposed strategy to target
426 certain regions close to the grid bar, since it still relies on visual/manual
427 selection. There is clearly a need for sophisticated automatic targeting tools on
428 grids prepared by spraying with sample droplets.
429
430 **Large required sample quantity.** Compared with conventional blotting
431 method, the TRCEM method requires a substantially bigger volume of sample
432 (~10 μL versus 3 μL) for each grid, which is the minimum quantity of fluid
433 required to reside in the whole microfluidic system for ensuring a stabilized
434 spray. However, much of the spray is wasted in the present setup with a single
435 EM grid as target, and an obvious next step is the development of a plunger
436 with multiple pairs of tweezers or a specially designed tweezer-manifold to
437 hold several grids at once.
438
439 **Unresolved questions regarding the mechanism of HflX action**. Our
440 TRCEM analysis about the interaction between HflX and 70S ribosome leaves
441 open the question of how HflX recognizes the stalled state of the ribosome.
442 Here our observation of 30S subunit head rotation from apo-70S to i70SHflX-
443 I may offer a clue. Puromysine-treated polysomes, having deacylated tRNA in
444 the P-site, display greatly enhanced HflX splitting activity, and this state was
445 proposed as the natural substrate for HflX[2]. In this state, the ribosome is known
446 to undergo spontaneous intersubunit rotation[34], which goes hand in hand with
447 30S subunit head 'swivel' rotation[35]. This would suggest that HflX initially
448 binds to the ribosome in its rotated conformation and forces it into the

449 unrotated conformation observed in i70SHflX-I, with residual 30S subunit
450 head rotation still retained. Another similarity holds if our hypothesis of HflX
451 binding to the rotated ribosome is correct since the latter is the substrate of
452 RRF/EF-G-GTP binding, as well[36,37]. But to answer these questions more
453 extensive studies with similar tools are required.
454
455
456
457
458
459
460
461
462
463
464
465
466
467
468
469
470
471
472
473
474
475
476
477
478

479 **FIGURES**

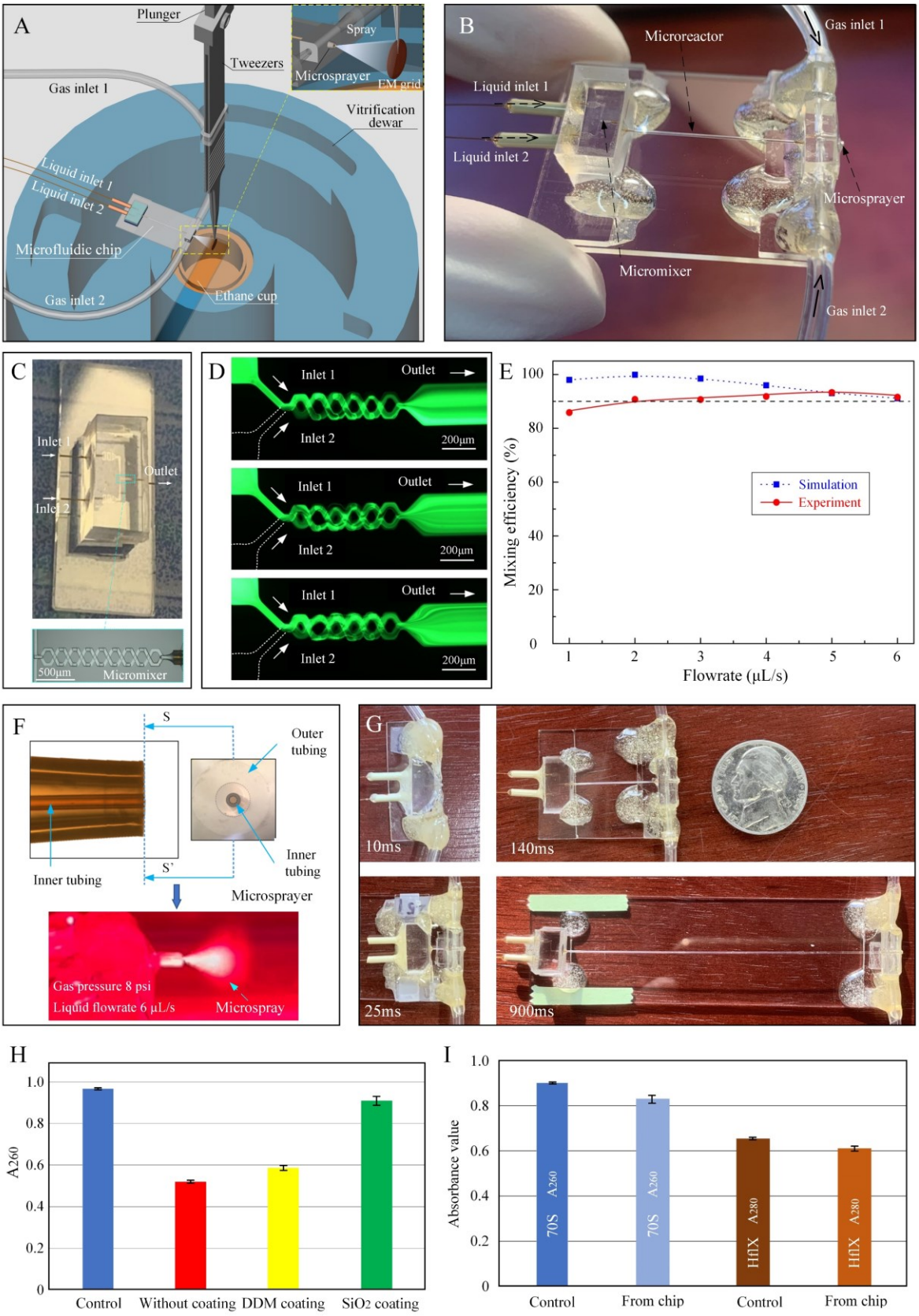

480

481 **Figure 1. The modular PDMS-based microfluidic chip assembly for TRCEM sample**
482 **preparation.** (A) Schematic showing the setup for TRCEM using the mixing-spraying-plunging
483 method. (B) The microfluidic chip assembly comprises three parts: micro-mixer, micro-reactor
484 and micro-sprayer. (C) The splitting-and-recombination (SAR) based micro-mixer is fabricated by
485 soft-lithography. (D) Fluorescence distribution along the micromixer with five mixing units under
486 different inlet flow rate conditions. The mixing efficiency is characterized by the evenness in the
487 distribution of fluorescent fluid. (E) Mixing efficiency for the micro-mixer at the exit under
488 different flow rate conditions. The high mixing performance of this micro-mixer was validated
489 both numerically and experimentally. (F) Micro-sprayer, with inner and outer tubing aligned and
490 centered, used for depositing the reaction product onto the grid. The micro-spray (illuminated by
491 red laser) is generated under the conditions of liquid flow rate 6 μL/s and gas pressure 8 psi, (G)
492 A set of microfluidic chips was employed to achieve required reaction time points of 10, 25, 140,
493 and 900 ms for the HflX study. (H) Compared with PDMS surface without any coating layer, and
494 with DDM coating, the SiO_2 coating shows effective mitigation of protein adsorption (*E. coli* 70S
495 is used as sample). (I) The SiO_2 coating functions well even after one month (here both *E. coli* 70S
496 and HflX are used as samples).

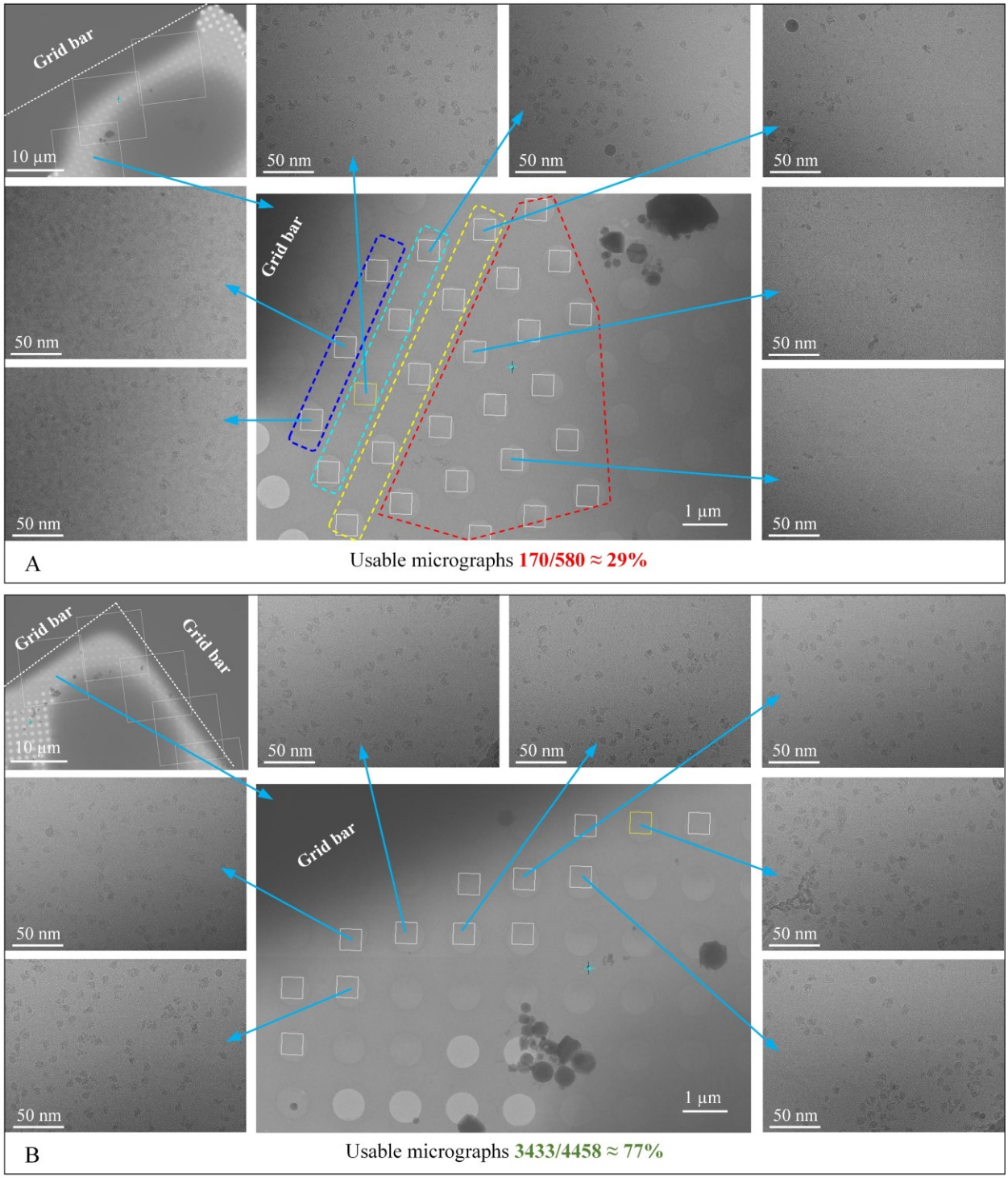

Figure 2. Data collection strategies on droplet-based cryo-grid prepared by mixing-spraying TRCEM method. (A) Collect as many micrographs as possible on each droplet. The number of particles gradually decreases when the target moves away from the grid bar, in the direction of

areas marked in blue, cyan, yellow and red. (B) Collect only along two or three lines of holes which are near and parallel to the grid bar.

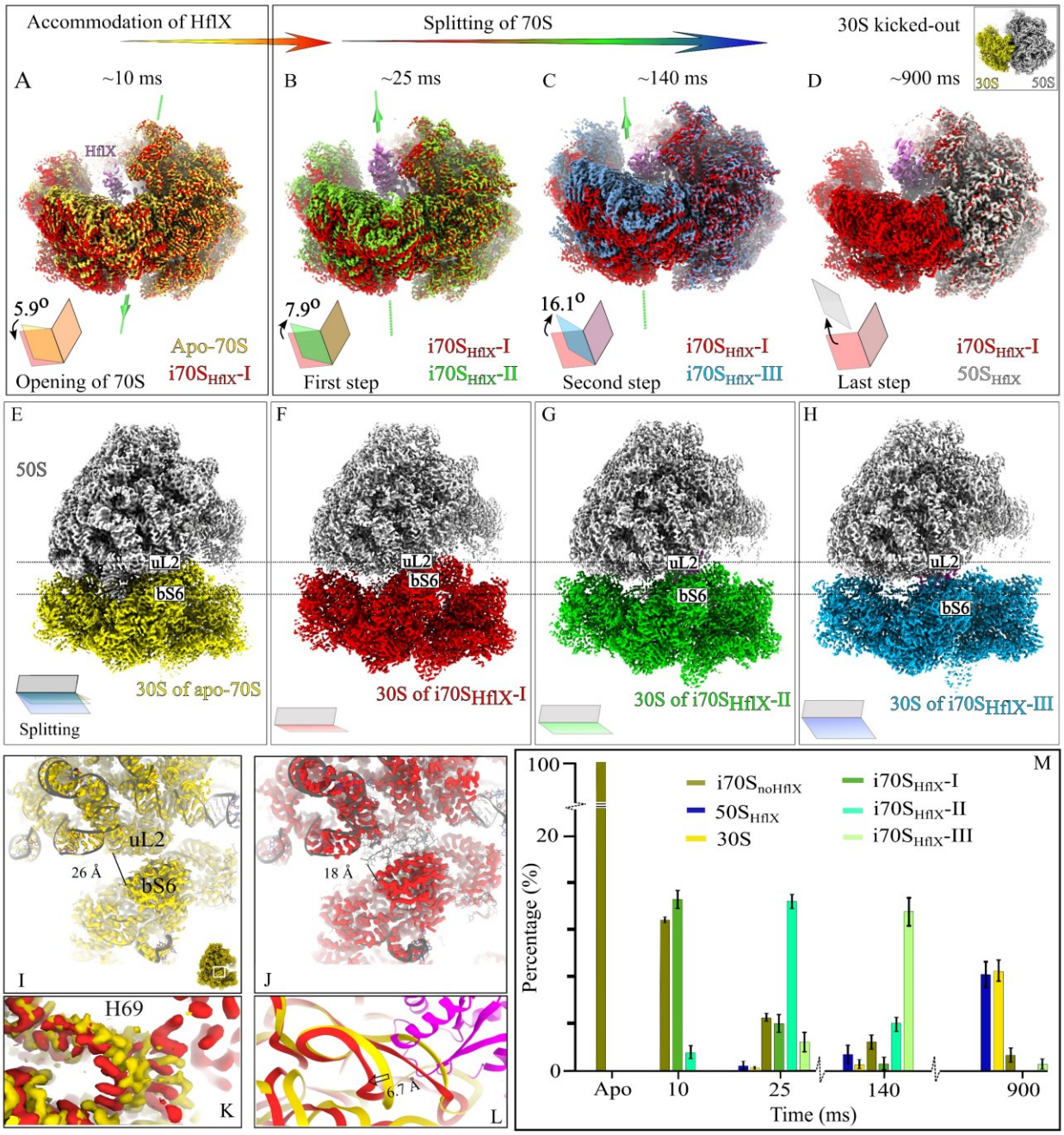

Figure 3. Molecular details of subunit interface during the progressive opening of the 70S (**A**) Superimposition of reconstructions to show the opening of the 30S subunit from apo-70S (yellow) to i70S$_{HflX}$-I (red) to accommodate HflX. The green line represents the initial axis of 30S rotation, Axis I. (**B**) and (**C**), reconstructions of second and third intermediates overlapped with first intermediate, showing the stepwise splitting of the 70S by HflX by rotation of the 30S subunit around Axis II (green line). The corresponding rotation angles and direction of 30S rotation are shown in cartoon book representations. (**D**), reconstruction of the 50S-HflX complex after the

517 departure of the 30S subunit, overlapped with the first 70S intermediate. In (**A**) through (**D**), all
518 reconstructions are aligned on the 50S subunit. (**E**) to (**H**) are the high-resolution densities of
519 control 70S at 900 ms and three intermediates obtained within 140 ms, and showing the stepwise
520 rotation of 30S during recycling with respect to 50S (gray). (**I**) and (**J**) are the zoomed views of
521 Coulomb densities in yellow for apo-70S and red for $i70S_{HflX}$-I, respectively, and corresponding
522 atomic models (gray) showing the rearrangement of the protein uL2 of the 50S and bS6 of 30S to
523 accommodate HflX. (**K**) and (**L**), Coulomb densities, and corresponding ribbon models of H69
524 from apo-70S (yellow), and $i70S_{HflX}$-I (red), respectively, showing the very first movement of
525 helix H69. HflX is shown in magenta. (**M**) Kinetics of the splitting reaction in terms of the number
526 of particles per class as a function of time, obtained by 3D classification.
527
528
529
530
531
532
533
534
535
536

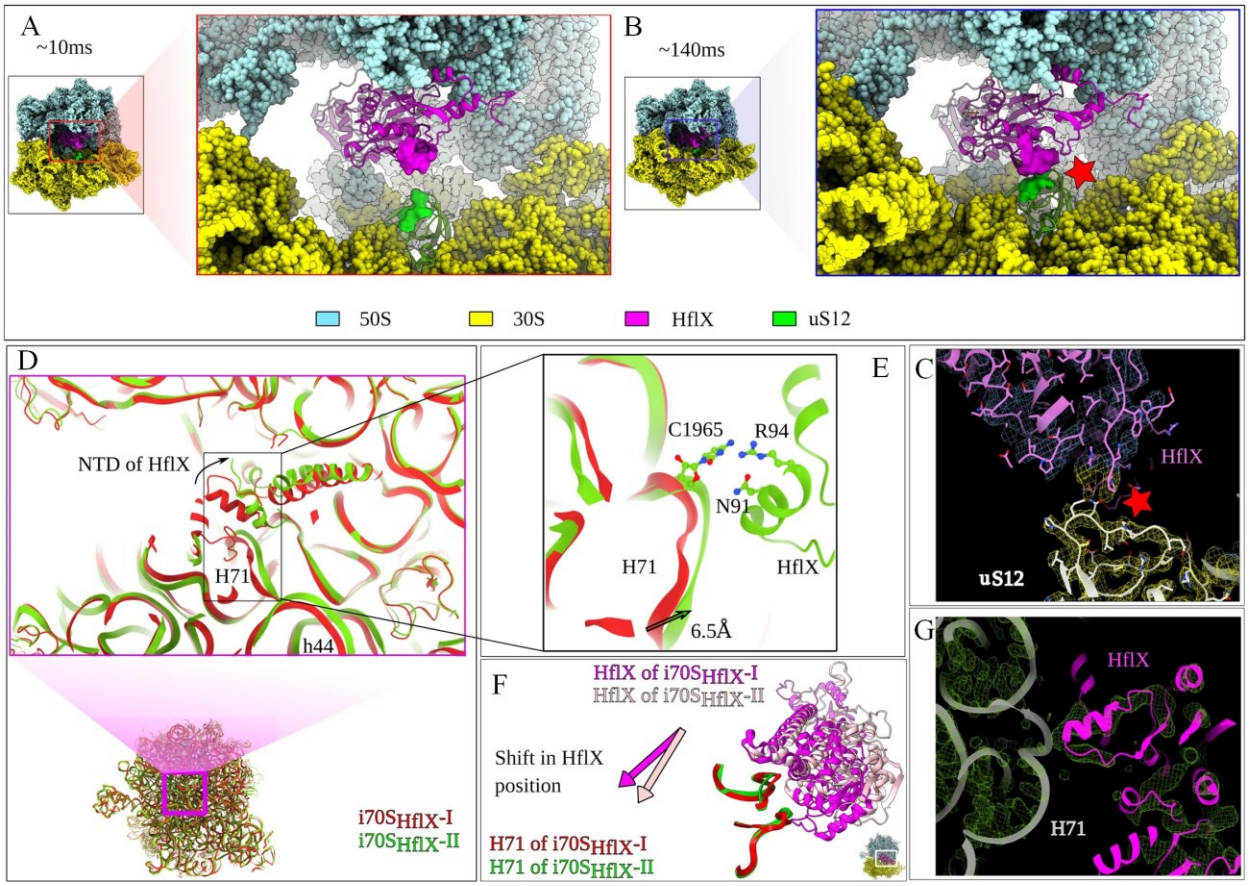

Figure 4. The shift of S12 towards HflX and Involvement of HflX in 70S splitting

The zoomed view of HflX and S12 of 30S interactions from i70SHflX-I and i70SHflX-III states are shown in (**A**) and (**B**), respectively. Due to the stepwise separation of the 30S during splitting, there occurs a steric clash (red star) at 140 ms due to the subsequent shift of the whole S12, which is not present at earlier states like10 ms, and this clash is the cause of the final separation of 30S from 50S by a power-stroke from HflX upon GTP hydrolysis. (**C**) The same clash at 140 ms from i70SHflX-III is shown in Coulomb density with a fitted model. (**D**) Pulling of H71 by the NTD of HflX causes the disruption of intersubunit bridge B3 between H71 and h44, and the zoomed view in (**E**) shows the interacting residues of both H71 and HflX. During pulling of H71 HflX has to shift its position and is shown in (**F**). (**G**) The same interaction is shown in Coulomb density with a fitted model.

552

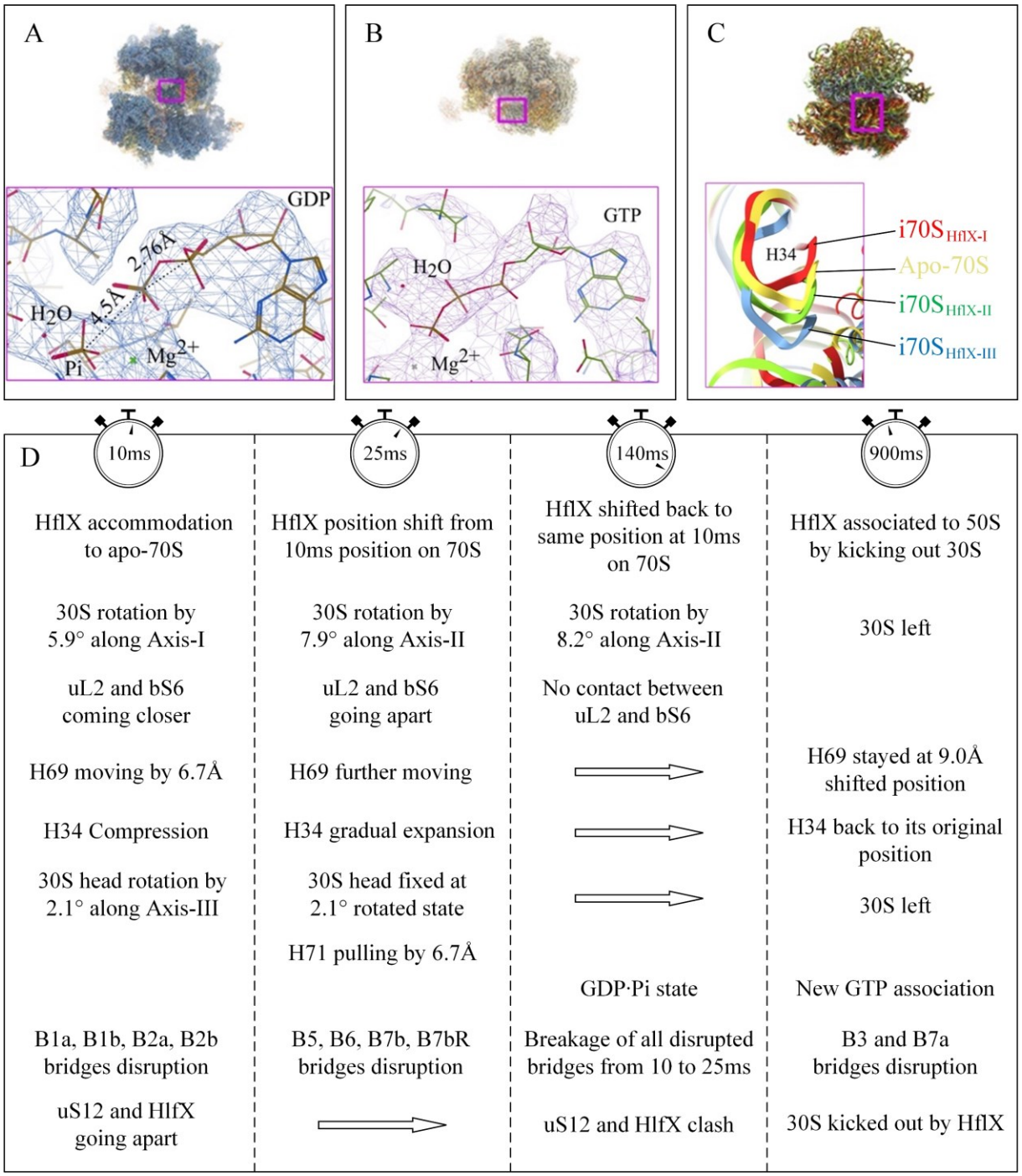

553

554 **Figure 5. Analysis of nucleotide states, and spring-like nature of H34 and molecular events**

555 (**A**) Refined density map of i70S$_{HflX}$-III (in mesh) with an atomic model fitted in with the zoomed

556 view of i70S$_{HflX}$-III with the fitted model of GTP • Pi. The distance of 4.5 Å between GDP and

557 Pi is compared with the distance of 2.8 Å between two P atoms of GDP. This distance between
558 GDP and Pi is too large to form a P-O bond as in GTP. (**B**) Refined density map of $50S_{HflX}$ (in
559 mesh) with atomic model fitted in along with the zoomed view of $50S_{HflX}$ with the fitted model of
560 GTP. (**C**) The superimposition of atomic models of apo-70S and three intermediates with the
561 zoomed view of H34 showing its spring-like behavior. Corresponding colors are indicated. (**D**)
562 The molecular events involved during the 70S splitting by HflX are tabulated.
563
564

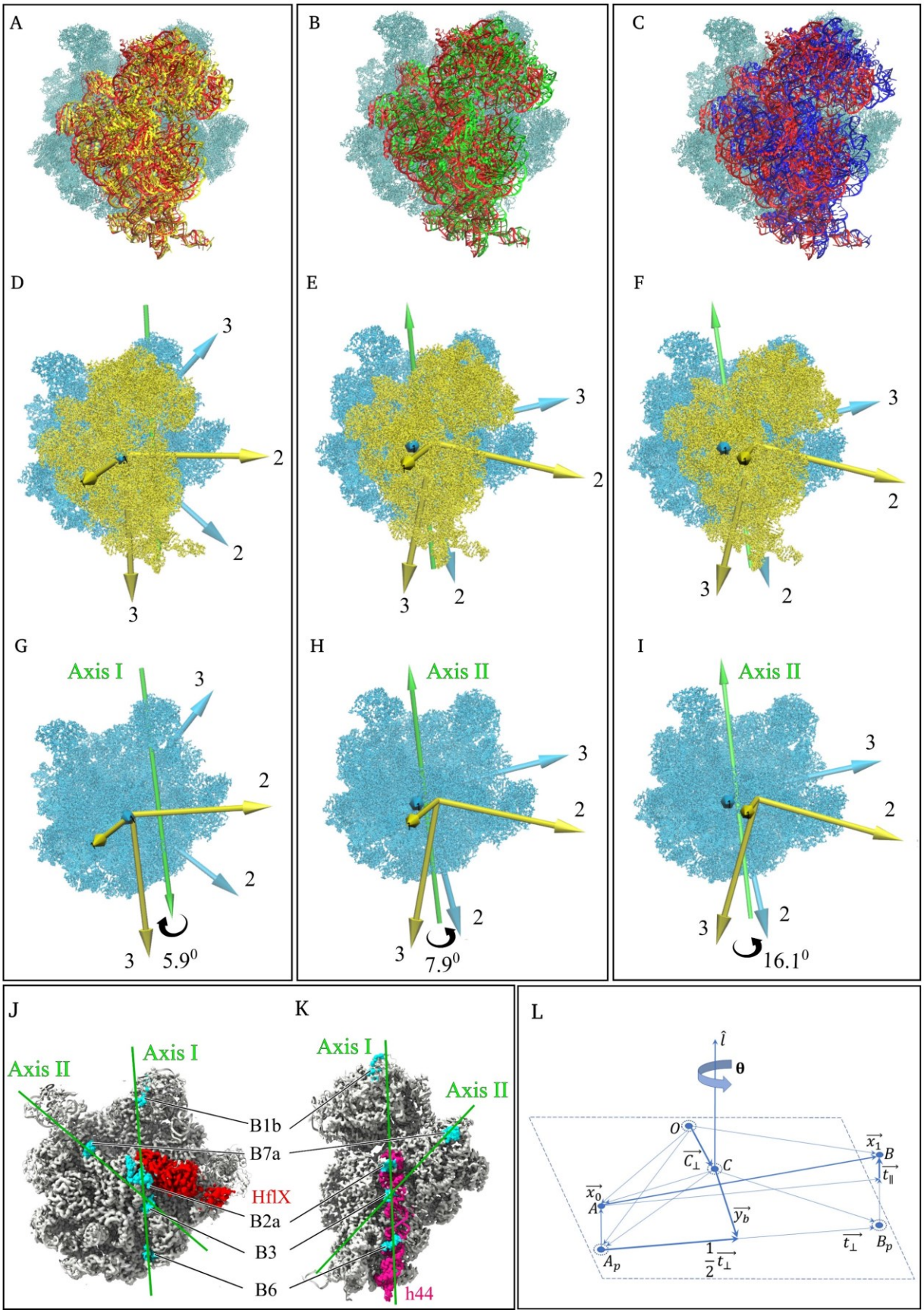
A
B
C
D
3
2
2
3
E
3
2
3
2
F
3
2
3
2
G
Axis I
3
2
2
3
5.9⁰
H
Axis II
3
2
2
3
7.9⁰
I
Axis II
3
2
2
3
16.1⁰
J
Axis II
Axis I
B1b
B7a
HflX
B2a
B3
B6
K
Axis I
Axis II
h44
L
$\hat{l}$
θ
O
C
$\overrightarrow{C_\perp}$
$\overrightarrow{x_1}$
B
$\overrightarrow{t_\parallel}$
$\overrightarrow{x_0}$
A
$\overrightarrow{y_b}$
A_p
$\frac{1}{2}\overrightarrow{t_\perp}$
$\overrightarrow{t_\perp}$
B_p

565

566 **Figure 6**. **Axes of rotation of 30S subunit during splitting/recycling of the 70S ribosome:** (**A**),
567 (**B**), and (**C**), rotation of 30S subunit from Apo-70S (yellow) to i70S$_{HflX}$-I (red), i70S$_{HflX}$-I (red) to
568 i70S$_{HflX}$-II (green), and i70S$_{HflX}$-I (red) to i70S$_{HflX}$-III (blue), respectively. **(D)**, **(E)**, and **(F)**
569 characterization of the 30S subunit rotation while the 50S subunits (cyan) are fixed in space. The
570 models show the rotated state of the 30S subunit in each case. For clarity, 30S subunits are
571 represented with only their principal axes of inertia. Rotation axes (Axis I, Axis II) are shown as
572 green arrows indicating the direction (right-hand thumb rule) of the rotation (black curled arrows).
573 **(D)** Rotation by 5.9° of 30S subunit around Axis I from Apo-70S (yellow) to i70S$_{HflX}$-I (red). (**E**)
574 and (**F**), Rotations by 7.9° and 16.1°, respectively, of 30S subunit around Axis II. **(G)**, **(H)**, and
575 **(I)**, same representation as **(D)**, **(E)**, and **(F)** omitting the 30S subunit to show the axes clearly. (**J**)
576 and (**K**), Intersubunit bridges through which Axes I and II pass on the 50S and 30S subunit,
577 respectively. **(L)** Formulation of rigid body motion along with location of the rotation axis. Initial
578 and transformed positions are respectively denoted by A (position vector $\vec{x}_0$) and B (position
579 vector $\vec{x}_1$). The shift from A to B is given by translation vector $\vec{t}$. Points with dotted circles are
580 on the plane perpendicular to the rotation axis $\hat{l}$. Points $\overrightarrow{A_p}$ and $\overrightarrow{B_p}$ are projections of points A
581 and B, respectively. $\vec{t}_{\parallel}$ and $\vec{t}_{\perp}$ are respectively the parallel and perpendicular components of the
582 translation vector $\vec{t}$. Axis $\hat{l}$ and angle θ describes the rotation of the rigid body from point A to B.
583 The rotation axis $\hat{l}$ passes through the point given by the position vector $\vec{C}_{\perp}$. The solution for the
584 position vector $\vec{C}_{\perp}$ is obtained by using the remaining vectors, as indicated in the derivation in
585 Methods Section in SI "Determining the position vector of the unique point through which the
586 rotation axis passes".
587
588
589
590 Supplemental video 1. Spraying and plunging during the TR experiment.
591
592 Supplemental video 2. The clamshell-like splitting of the ribosome from Intermediate I over
593 Intermediates II and III, ending with the 50S subunit (shown) and the 30S subunit (not shown), the
594 end products of the recycling process.
595

Acknowledgements

This work was supported by a grant from the National Institutes of Health R35GM139453 (to J.F.). All data was collected at the Columbia University Cryo-Electron Microscopy Center (CEC). We thank Robert A. Grassucci, and Yen-Hong Kao for their help with the cryo-EM data collection. The microfluidic chips with SiO_2 coating were fabricated in Nanofabrication clean room facility in Columbia University.

Author contributions

S.B., X.F., and J.F. conceived the research; S.B., X.F., and J.F. designed the experiments; S.B. prepared the biological samples; X.F. designed the TR chips; X.F., and P.D., developed the chip; X.F., S.B., performed the TR cryo-EM experiments; S.B., X.F., and Z.Z. collected the Cryo-EM data; S.B. processed the data; S.M. calculated the subunit and domain motions and the axes of rotation; Z.P.B. helped S.B. with atomic model building and validation, S.B., X.F., and J.F. wrote the manuscript with the help of S.M. for Methods.

Declaration of interest

Columbia University has filed patent applications related to this work for which X.F. and J.F. are inventors.

Data and code availability

The refined maps are deposited on EMDB and corresponding atomic models on PDB and will be publicly available as of the date of publication.

621 EMD-29681 (control apo-70S at 900ms), 29688 (i70S$_{HflX}$-I), 29687 (i70S$_{HflX}$-
622 II), 29689 (i70S$_{HflX}$-III), 29833 (consensus i70S$_{HflX}$-I, 30S focused), 29834
623 (i70S$_{HflX}$-I, 50S focused and 30S subtracted), 29724 (consensus i70S$_{HflX}$-II, 30S
624 focused), 29844 (i70S$_{HflX}$-II, 50S focused and 30S subtracted), 29723 (consensus
625 i70S$_{HflX}$-III, 30S focused), 29842 (i70S$_{HflX}$-III, 50S focused and 30S subtracted).
626
627 PDB- 8G2U (control apo-70S at 900ms), 8G34 (i70S$_{HflX}$-I), 8G31 (i70S$_{HflX}$-II),
628 8G38 (i70S$_{HflX}$-III).
629
630 **References:**

631 1. Gao, N., Zavialov, A.V., Li, W., Sengupta, J., Valle, M., Gursky, R.P.,
632 Ehrenberg, M., and Frank, J. (2005). Mechanism for the disassembly of the
633 posttermination complex inferred from cryo-EM studies. Mol Cell *18*, 663-
634 674. https://doi.org/10.1016/j.molcel.2005.05.005.

635 2. Zhang, Y., Mandava, C.S., Cao, W., Li, X., Zhang, D., Li, N., Zhang, Y.,
636 Zhang, X., Qin, Y., Mi, K., et al. (2015). HflX is a ribosome-splitting factor
637 rescuing stalled ribosomes under stress conditions. Nat Struct Mol Biol *22*,
638 906-913. https://doi.org/10.1038/nsmb.3103.

639 3. Koripella, R.K., Deep, A., Agrawal, E.K., Keshavan, P., Banavali, N.K., and
640 Agrawal, R.K. (2021). Distinct mechanisms of the human mitoribosome
641 recycling and antibiotic resistance. Nat Commun *12*, 3607.
642 https://doi.org/10.1038/s41467-021-23726-4.

643 4. Brito Querido, J., Sokabe, M., Kraatz, S., Gordiyenko, Y., Skehel, J.M.,
644 Fraser, C.S., and Ramakrishnan, V. (2020). Structure of a human 48S
645 translational initiation complex. Science *369*, 1220-1227.
646 https://doi.org/10.1126/science.aba4904.

647 5. Frank, J. (2017). Time-resolved cryo-electron microscopy: Recent progress.
648 J Struct Biol *200*, 303-306. https://doi.org/10.1016/j.jsb.2017.06.005.

649 6. Chen, B., and Frank, J. (2016). Two promising future developments of cryo-
650 EM: capturing short-lived states and mapping a continuum of states of a
651 macromolecule. Microscopy (Oxf) *65*, 69-79.
652 https://doi.org/10.1093/jmicro/dfv344.

653 7. Dandey, V.P., Budell, W.C., Wei, H., Bobe, D., Maruthi, K., Kopylov, M.,
654 Eng, E.T., Kahn, P.A., Hinshaw, J.E., Kundu, N., et al. (2020). Time-
655 resolved cryo-EM using Spotiton. Nat Methods *17*, 897-900.
656 https://doi.org/10.1038/s41592-020-0925-6.

657 8. Chen, B., Kaledhonkar, S., Sun, M., Shen, B., Lu, Z., Barnard, D., Lu, T.M.,
658 Gonzalez, R.L., Jr., and Frank, J. (2015). Structural dynamics of ribosome
659 subunit association studied by mixing-spraying time-resolved cryogenic
660 electron microscopy. Structure *23*, 1097-1105.
661 https://doi.org/10.1016/j.str.2015.04.007.

662 9. Fu, Z., Kaledhonkar, S., Borg, A., Sun, M., Chen, B., Grassucci, R.A.,
663 Ehrenberg, M., and Frank, J. (2016). Key Intermediates in Ribosome
664 Recycling Visualized by Time-Resolved Cryoelectron Microscopy.
665 Structure *24*, 2092-2101. https://doi.org/10.1016/j.str.2016.09.014.

666 10. Kaledhonkar, S., Fu, Z., Caban, K., Li, W., Chen, B., Sun, M., Gonzalez,
667 R.L., Jr., and Frank, J. (2019). Late steps in bacterial translation initiation
668 visualized using time-resolved cryo-EM. Nature *570*, 400-404.
669 https://doi.org/10.1038/s41586-019-1249-5.

670 11. Kaledhonkar, S., Fu, Z., White, H., and Frank, J. (2018). Time-Resolved
671 Cryo-electron Microscopy Using a Microfluidic Chip. Methods Mol Biol
672 *1764*, 59-71. https://doi.org/10.1007/978-1-4939-7759-8_4.

673 12. Klebl, D.P., White, H.D., Sobott, F., and Muench, S.P. (2021). On-grid and
674 in-flow mixing for time-resolved cryo-EM. Acta Crystallogr D Struct Biol
675 *77*, 1233-1240. https://doi.org/10.1107/S2059798321008810.

676 13. Maeots, M.E., Lee, B., Nans, A., Jeong, S.G., Esfahani, M.M.N., Ding, S.,
677 Smith, D.J., Lee, C.S., Lee, S.S., Peter, M., and Enchev, R.I. (2020).
678 Modular microfluidics enables kinetic insight from time-resolved cryo-EM.
679 Nat Commun *11*, 3465. https://doi.org/10.1038/s41467-020-17230-4.

680 14. Kontziampasis, D., Klebl, D.P., Iadanza, M.G., Scarff, C.A., Kopf, F.,
681 Sobott, F., Monteiro, D.C.F., Trebbin, M., Muench, S.P., and White, H.D.

682 (2019). A cryo-EM grid preparation device for time-resolved structural
683 studies. IUCrJ *6*, 1024-1031. https://doi.org/10.1107/S2052252519011345.

684 15. Berriman, J., and Unwin, N. (1994). Analysis of transient structures by cryo-
685 microscopy combined with rapid mixing of spray droplets. Ultramicroscopy
686 *56*, 241-252. https://doi.org/10.1016/0304-3991(94)90012-4.

687 16. Lu, Z., Shaikh, T.R., Barnard, D., Meng, X., Mohamed, H., Yassin, A.,
688 Mannella, C.A., Agrawal, R.K., Lu, T.M., and Wagenknecht, T. (2009).
689 Monolithic microfluidic mixing-spraying devices for time-resolved cryo-
690 electron microscopy. J Struct Biol *168*, 388-395.
691 https://doi.org/10.1016/j.jsb.2009.08.004.

692 17. Lu, Z., Barnard, D., Shaikh, T.R., Meng, X., Mannella, C.A., Yassin, A.,
693 Agrawal, R., Wagenknecht, T., and Lu, T.M. (2014). Gas-Assisted Annular
694 Microsprayer for Sample Preparation for Time-Resolved Cryo-Electron
695 Microscopy. J Micromech Microeng *24*, 115001.
696 https://doi.org/10.1088/0960-1317/24/11/115001.

697 18. Knoska, J., Adriano, L., Awel, S., Beyerlein, K.R., Yefanov, O., Oberthuer,
698 D., Pena Murillo, G.E., Roth, N., Sarrou, I., Villanueva-Perez, P., et al.
699 (2020). Ultracompact 3D microfluidics for time-resolved structural biology.
700 Nat Commun *11*, 657. https://doi.org/10.1038/s41467-020-14434-6.

701 19. Torino, S., Dhurandhar, M., Stroobants, A., Claessens, R., and Efremov,
702 R.G. (2022). Time-resolved cryo-EM using a combination of droplet
703 microfluidics with on-demand jetting. bioRxiv, 2022.2010. 2021.513149.
704 https://doi.org/10.1101/2022.10.21.513149.

705 20. Noble, A.J., Dandey, V.P., Wei, H., Brasch, J., Chase, J., Acharya, P., Tan,
706 Y.Z., Zhang, Z., Kim, L.Y., and Scapin, G. (2018). Routine single particle
707 CryoEM sample and grid characterization by tomography. Elife *7*, e34257.

708 21. Verstraeten, N., Fauvart, M., Versees, W., and Michiels, J. (2011). The
709 universally conserved prokaryotic GTPases. Microbiol Mol Biol Rev *75*,
710 507-542, second and third pages of table of contents.
711 https://doi.org/10.1128/MMBR.00009-11.

712 22. Coatham, M.L., Brandon, H.E., Fischer, J.J., Schummer, T., and Wieden,
713 H.J. (2016). The conserved GTPase HflX is a ribosome splitting factor that
714 binds to the E-site of the bacterial ribosome. Nucleic Acids Res *44*, 1952-
715 1961. https://doi.org/10.1093/nar/gkv1524.

716 23. Rudra, P., Hurst-Hess, K.R., Cotten, K.L., Partida-Miranda, A., and Ghosh,
717 P. (2020). Mycobacterial HflX is a ribosome splitting factor that mediates
718 antibiotic resistance. Proceedings of the National Academy of Sciences *117*,
719 629-634.

720 24. Dey, S., Biswas, C., and Sengupta, J. (2018). The universally conserved
721 GTPase HflX is an RNA helicase that restores heat-damaged Escherichia
722 coli ribosomes. J Cell Biol *217*, 2519-2529.
723 https://doi.org/10.1083/jcb.201711131.

724 25. Feng, X., Fu, Z., Kaledhonkar, S., Jia, Y., Shah, B., Jin, A., Liu, Z., Sun, M.,
725 Chen, B., Grassucci, R.A., et al. (2017). A Fast and Effective Microfluidic
726 Spraying-Plunging Method for High-Resolution Single-Particle Cryo-EM.
727 Structure *25*, 663-670.e663. https://doi.org/10.1016/j.str.2017.02.005.

728 26. Hirokawa, G., Iwakura, N., Kaji, A., and Kaji, H. (2008). The role of GTP in
729 transient splitting of 70S ribosomes by RRF (ribosome recycling factor) and
730 EF-G (elongation factor G). Nucleic Acids Res *36*, 6676-6687.
731 https://doi.org/10.1093/nar/gkn647.

732 27. Frank, J., and Agrawal, R.K. (2000). A ratchet-like inter-subunit
733 reorganization of the ribosome during translocation. Nature *406*, 318-322.
734 https://doi.org/10.1038/35018597.

735 28. Maji, S., Shahoei, R., Schulten, K., and Frank, J. (2017). Quantitative
736 Characterization of Domain Motions in Molecular Machines. J Phys Chem
737 B *121*, 3747-3756. https://doi.org/10.1021/acs.jpcb.6b10732.

738 29. Simsir, M., Broutin, I., Mus‐Veteau, I., and Cazals, F. (2021). Studying
739 dynamics without explicit dynamics: A structure‐based study of the export
740 mechanism by AcrB. Proteins: structure, function, and bioinformatics *89*,
741 259-275. https://doi.org/10.1002/prot.26012.

742 30. Gangwar, S.P., Yen, L.Y., Yelshanskaya, M.V., and Sobolevsky, A.I.
743 (2023). Positive and negative allosteric modulation of GluK2 kainate
744 receptors by BPAM344 and antiepileptic perampanel. Cell Reports *42*.
745 https://doi.org/10.1016/j.celrep.2023.112124.

746 31. Qiu, W., Fu, Z., Xu, G.G., Grassucci, R.A., Zhang, Y., Frank, J.,
747 Hendrickson, W.A., and Guo, Y. (2018). Structure and activity of lipid
748 bilayer within a membrane-protein transporter. Proceedings of the National

749 Academy of Sciences *115*, 12985-12990.
750 https://doi.org/10.1073/pnas.1812526115.

751 32. Harder, O.F., Barrass, S.V., Drabbels, M., and Lorenz, U.J. (2023). Fast
752 viral dynamics revealed by Microsecond Time-Resolved Cryo-EM. bioRxiv,
753 2023.2004. 2019.536710.

754 33. Voss, J.M., Harder, O.F., Olshin, P.K., Drabbels, M., and Lorenz, U.J.
755 (2021). Rapid melting and revitrification as an approach to microsecond
756 time-resolved cryo-electron microscopy. Chemical Physics Letters *778*,
757 138812.

758 34. Valle, M., Zavialov, A., Sengupta, J., Rawat, U., Ehrenberg, M., and Frank,
759 J. (2003). Locking and unlocking of ribosomal motions. Cell *114*, 123-134.
760 https://doi.org/10.1016/s0092-8674(03)00476-8.

761 35. Ratje, A.H., Loerke, J., Mikolajka, A., Brünner, M., Hildebrand, P.W.,
762 Starosta, A.L., Dönhöfer, A., Connell, S.R., Fucini, P., and Mielke, T.
763 (2010). Head swivel on the ribosome facilitates translocation by means of
764 intra-subunit tRNA hybrid sites. Nature *468*, 713-716.
765 https://doi.org/10.1038/nature09547.

766 36. Agrawal, R.K., Sharma, M.R., Kiel, M.C., Hirokawa, G., Booth, T.M.,
767 Spahn, C.M., Grassucci, R.A., Kaji, A., and Frank, J. (2004). Visualization
768 of ribosome-recycling factor on the Escherichia coli 70S ribosome:
769 functional implications. Proceedings of the National Academy of Sciences
770 *101*, 8900-8905. https://doi.org/10.1073/pnas.0401904101.

771 37. Dunkle, J.A., Wang, L., Feldman, M.B., Pulk, A., Chen, V.B., Kapral, G.J.,
772 Noeske, J., Richardson, J.S., Blanchard, S.C., and Cate, J.H.D. (2011).
773 Structures of the bacterial ribosome in classical and hybrid states of tRNA
774 binding. Science *332*, 981-984. https://doi.org/10.1126/science.1202692.
775